Automation in Construction 180 (2025) 106508

Contents lists available at ScienceDirect

Automation in Construction

journal homepage: www.elsevier.com/locate/autcon

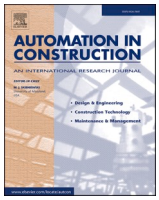

Design and construction of an asymptotic kinetic transformable canopy

Zongshuai Wan [a,b], Haotian Man [a,b], Kristof Crolla [a], Eike Schling [b,*]

[a] The University of Hong Kong, Department of Architecture, Hong Kong, China
[b] Leibniz University Hannover, Faculty of Architecture and Landscape Sciences, Hannover, Germany

ARTICLE INFO

Keywords:
Kinetic structures
Asymptotic network
Architectural geometry
Transformable structures
Optimization
Actuation system

ABSTRACT

Transformable structures offer significant potential for adaptive and deployable architecture but face challenges of complex fabrication and actuation. This paper addresses the design and construction of kinetic grid structures using asymptotic curve networks, enabling the creation of doubly curved gridshells from straight, elastic Glass Fiber Reinforced Polymer (GFRP) planks. Connected by standardised scissor joints, the planks undergo controlled transformation through elastic deformation. The design process integrates differential geometry and discrete mesh optimization to define and simulate the structure's behaviour. A full-scale prototype—the *Kinetic Canopy*—was fabricated and transformed from a flat configuration into an arched gridshell using an integrated cable actuation system, without support movements. The transformation was analysed using a non-linear finite element model and validated against physical experiments. The paper provides a detailed evaluation of initial stresses, actuation forces, and energy shifts, establishing a comprehensive framework for the design and analysis of asymptotic kinetic structures.

1. Introduction

Transformable structures are capable of adapting their shape to internal and external conditions and functional needs [1], and offer opportunities for retrofitting building envelopes, creating adaptive roofs and weather protection in urban environments [2–4].

The elastic deformation of structural components has been utilized for transformable architectural applications. Schleicher [5] explored the principles of motion in flexible plant movements and applied them to innovative kinetic architectural designs. Soriano [6] carried on the physical and experimental investigation of deployable geodesic gridshells (G-Shells), which originate from a flat and compact grid of flat strips. Pauly [7] harnessed the geometric incoherence of variable-pitch scissor-hinge mechanisms to design and fabricate X-Shells. Bi [8] examined elastica-ruled surfaces and suggested designing kinetic structures by combining a series of non-intersecting, elastically bent thin strips. Tellier [9,10] developed bundling elastic gridshells with alignable nets for easier deployment and off-site fabrication. Pellis [11] introduced alignable lamella gridshells capable of collapsing into planar strips, enhancing transportation and installation efficiency.

In recent years, the field of architectural geometry [12] has introduced innovative methods for designing doubly curved grids using straight, elastic planks [13]. Schling proposed the design and construction of asymptotic structures [14], along the asymptotic curves with zero normal curvature on a smooth surface. To achieve the desired design geometry, straight planks are strategically positioned vertically in a grid, relying on twisting and bending around their weak profile axis. This strategy has since been employed in various architectural applications and research projects, such as the Inside/Out pavilion in Munich [15], the Intergroup Hotel Canopy in Ingolstadt [16], the Curtain Wall System in Hong Kong [17–19], and the Asymptotic Geodesic Hybrid Timber Gridshell in Munich [20,21]. Based on this research, Wang [22] proposed propagation algorithms to design asymptotic geodesic hybrid gridshells. The elastic kinetic behaviour of asymptotic grids has provided a novel perspective for designing transformable structures. Schikore employed isogeometric analysis (IGA) [23] to simulate the kinetic properties of asymptotic structures [24]. Furthermore, Schling and Schikore conducted a study exploring the influence of grid morphology on the kinetic behaviour of asymptotic networks [25]. In 2021, the first kinetic asymptotic structure, known as Kinetic Umbrella, was designed

* Corresponding author.
E-mail addresses: wanzs@hku.hk (Z. Wan), kcrolla@hku.hk (K. Crolla), schling@iek.uni-hannover.de (E. Schling).

https://doi.org/10.1016/j.autcon.2025.106508
Received 20 February 2025; Received in revised form 27 August 2025; Accepted 1 September 2025
Available online 13 September 2025

and constructed in Munich [26]. The rotational symmetric system transforms from a cylinder into a cantilevering "flower"-shape. The transformation relies on a combination of scissor hinges and element deformation. The kinetic motions take advantage of the gravitational force to open and close, using ring cables to fix and contract.

Despite considerable advancements in the topic of asymptotic kinetic structures, certain research gaps still exist. Existing research on asymptotic kinetic grids primarily adopts rotationally symmetrical forms. This highlights the necessity for more in-depth investigations into complex open geometry designs that allow greater design freedom and transformations from planar to doubly curved configurations, thereby potentially broadening architectural possibilities. Furthermore, although current grid designs for sculpture structures serve their intended purposes effectively, room exists for improvement in terms of rigidity and versatility, enhancing their suitability as sturdy and reliable roofing structures. Additionally, there is a need for further research into integrated actuation systems. A more comprehensive understanding of the impact of friction, initial stress, and gravity on kinetic transformations is imperative.

Contributions: The study presents a discrete optimization method utilizing theories from differential geometry to design asymptotic grids and forecast its transformation characteristics. Geometrical analysis is used to predict strain energies throughout the transformation process. The computational design workflow is validated through a physical prototype. The Kinetic Canopy, with 6 m span, is built from elastic, straight GFRP planks. Through the strategic placement of supports, scissor joints, and a pulley system functioning as a driving cable within the grid, the structure can be accurately transformed along a desired path. The transformation process is analysed using a non-linear FE simulation, enabling accurate evaluation of structural response under the actuation action. A comparative assessment of the three core methods—geometric optimization, physical prototyping, and FE simulation—demonstrates their respective accuracies and roles within the integrated design-to-construction process. This research contributes to the advancement of kinetic canopy structures, furnishing a comprehensive design and construction methodology for their deployment.

Section 2 provides a comprehensive overview of the geometric fundamentals relevant to our study, explains the optimization method and initial geometry generation of the kinetic asymptotic canopy, and outlines various service shapes. Section 3 delves into the construction process of the kinetic canopy, detailing elements such as plank and joint development, prefabrication and assembly, support design, actuation system, and strategies for stabilization/bracing. Section 4 introduces a non-linear finite element modelling approach including the prototype, supports, actuation system, and initial stress. Lastly, Section 5 discusses the research findings, with a focus on transformation process, actuation forces, energy variation and offers a vision for architectural scenarios.

2. Computational geometry design

The design of the kinetic canopy is rooted in the geometric properties of asymptotic curves on surfaces. This section outlines the fundamental principles of curves on surfaces, the discrete optimization method used to generate the asymptotic network, and the definition of various service stages for the transformable structure.

2.1. Curves on surfaces

There is a neat relationship between the elastic deformations of a slender plank within a gridshell and the curvature of respective curves on a surface network in differential geometry. As illustrated in Fig. 1, the local elastic deformation within an initially straight plank can be characterized at any position as embedded bending around the weak z-axis, bending around the strong y-axis, and twisting around the x-axis. For any curve on a surface [27], three specific curvatures can be determined using the local coordinate system known as the Darboux Frame: The

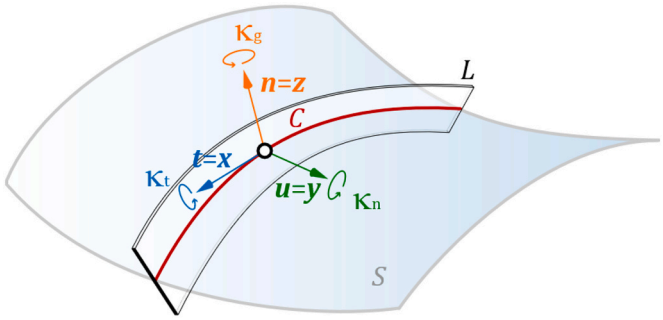

Fig. 1. Three curvatures of a curve on a surface: geodesic curvature κ_g, geodesic torsion κ_t and normal curvature κ_n [17].

geodesic curvature κ_g is measured around the local normal vector $\boldsymbol{n}$ of the surface, the geodesic torsion[1] κ_t is measured around the tangent vector $\boldsymbol{t}$ of the curve, and the normal curvature κ_n is measured around their cross-product $\boldsymbol{u} = \boldsymbol{t} \times \boldsymbol{n}$ [28]. The structural elements L align with the surface and curve orientation, ensuring that beam local axes $\boldsymbol{x}$, $\boldsymbol{y}$ and $\boldsymbol{z}$ correspond to $\boldsymbol{t}$, $\boldsymbol{u}$ and $\boldsymbol{n}$. Consequently, any geometric curvature can be assumed equivalent to the initial physical bending of the planks.

By designing a structure along specific paths that eliminate one of these curvatures, the elements and joints can be significantly simplified. Asymptotic curves follow the path of zero normal curvature ($\kappa_n = 0$), meaning that a linear plank can be bent and twisted along this path while maintaining its strong, bending stiffness around axis y.

2.2. Discrete network and optimization

This section details the discrete optimization process used to generate an initial asymptotic network. The objective is to create a grid that conforms to specific geometric relationships under given boundary conditions (planar supports). While the general method is applicable to any negatively curved surface [29], we demonstrate its specific application here through the design of our arch-shaped kinetic prototype.

The workflow for generating the asymptotic network, illustrated in Fig. 2, began with the definition of an initial arch-shaped NURB surface S exhibiting full symmetry along both principal in-plane directions, defined by 9 control points (a). This surface was then uniformly discretized into a quadrilateral mesh M with 52 longitudinal and 32 transverse segments (b). To approximate asymptotic directions, diagonals were introduced within each quadrilateral cell, forming a diamond mesh pattern. These diagonal segments were subsequently optimized to follow asymptotic curves using local constraints based on the method by Tang et al. [30]. Additionally, a unit normal vector was established at each mesh vertex, with both vertex coordinates ($\boldsymbol{v}_i$) and their corresponding normal vectors ($\boldsymbol{n}_i$) treated as optimization variables. The asymptotic network was finally obtained by solving the optimization problem using the following constraints, resulting in two families of asymptotic curves and positioning of the optimized vertices (c).

The asymptotic constraint is formulated as a curvature-based term that enforces the key geometric property of *asymp*totic curves: the normal curvature must be zero. This is achieved by ensuring each polyline segment is perpendicular to the surface normals at its endpoints (Fig. 3). The constraint is mathematically defined as:

$$C_{\mathrm{A-net}} = \sum_{i=1}^{N_{\mathrm{asym}}} (\boldsymbol{n}_{\mathrm{ia}} \bullet (\boldsymbol{v}_{\mathrm{ia}} - \boldsymbol{v}_{\mathrm{ib}}))^2 + (\boldsymbol{n}_{\mathrm{ib}} \bullet (\boldsymbol{v}_{\mathrm{ia}} - \boldsymbol{v}_{\mathrm{ib}}))^2 \quad (1)$$

[1] The geodesic torsion is commonly denoted as τ_g in the field of Architectural Geometry; however, in this paper, we use κ_t instead to avoid confusion with the symbol for shear stress.

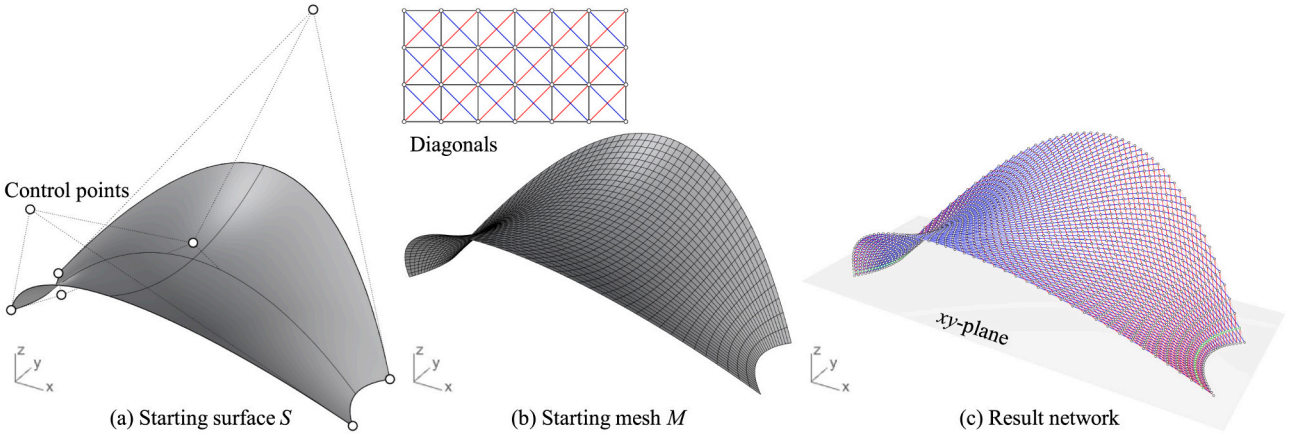

Fig. 2. Generation of asymptotic network through discretization and optimization: (a) Initial NURB surface; (b) Quad mesh with asymptotic diagonals; (c) Optimized asymptotic network.

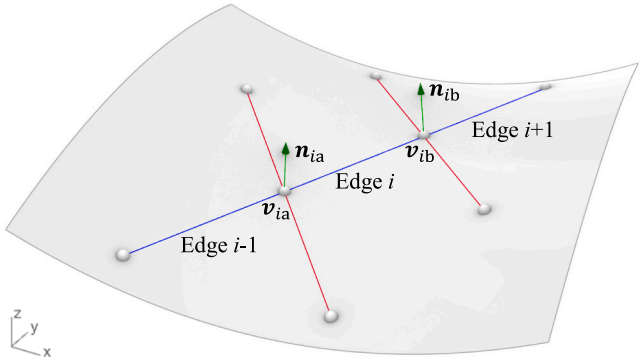

Fig. 3. Geometric definition of discrete asymptotic polylines (red and blue) and normals (green). (For interpretation of the references to colour in this figure legend, the reader is referred to the web version of this article.)

where, $\boldsymbol{n}_{ia}$ and $\boldsymbol{n}_{ib}$ are the normal vectors at the end vertices $\boldsymbol{v}_{ia}$ and $\boldsymbol{v}_{ib}$, respectively, for the i-th asymptotic segment (Edge i). Here, N_{asym} represents the total number of asymptotic segments in the mesh.

Simultaneously, a normalization constraint is applied to all the normal vectors within the discrete network [28,30]. This is mathematically represented as:

$$C_{norm} = \sum_{i=1}^{N_{vertex}} (\boldsymbol{n}_i \bullet \boldsymbol{n}_i - 1)^2 \tag{2}$$

where, $\boldsymbol{n}_i$ denotes the normal vector at the vertex $\boldsymbol{v}_i$, and N_{vertex} represents the total number of vertices. This constraint ensures that each normal vector maintains a unit length, thereby preserving the uniformity and regularity of the network.

These two formulas are the most basic constraints that satisfy the asymptotic curve characteristics.

To make the generated mesh smoother and prevent distortion, fairness constraints can be applied to all asymptotic polylines:

$$C_{fair} = \sum_{i \in poly} \|2\boldsymbol{v}_i - \boldsymbol{v}_{i-1} - \boldsymbol{v}_{i+1}\|^2 \tag{3}$$

where, $\boldsymbol{v}_{i-1}$, $\boldsymbol{v}_i$, $\boldsymbol{v}_{i+1}$ are any three consecutive points on the same asymptotic polylines. Minimizing this expression encourages asymptotic polylines to straighten, effectively acting as a discrete approximation of a bending-minimizing constraint.

In addition, the positions of specific points can be adjusted to accommodate architectural or construction requirements. In the given scenario, as depicted in Fig. 2c, the green points are aligned to the ground level (xy-plane). Subsequently, the boundary constraints can be implemented as follows:

$$C_{boundary} = \sum_{i \in boundary} (\boldsymbol{v}_i \bullet [0, 0, 1])^2 \tag{4}$$

where, $\boldsymbol{v}_i$ is the vertex on the boundary.

The comprehensive objective function, aggregating various constraints with penalty weights, is conceptualized as a non-linear least-squares problem:

$$F(\boldsymbol{X}) = C_{A-net}(\boldsymbol{X}) + C_{norm}(\boldsymbol{X}) + C_{boundary}(\boldsymbol{X}) + bC_{fair}(\boldsymbol{X}) \tag{5}$$

where $\boldsymbol{X}$ represents the variable vector encompassing all vertex coordinates $\boldsymbol{v}_i$ and their corresponding normal vectors $\boldsymbol{n}_i$.

This formulation aims to compute the optimal $\boldsymbol{X}$ that minimizes $F(\boldsymbol{X})$. The Trust Region Reflective algorithm [31] is employed to solve this optimization, with coefficients of the constraint terms carefully calibrated to preserve the geometric quality of the network. The penalty weights for the geometric constraint terms C_{A-net}, C_{norm}, and $C_{boundary}$ are fixed at 1.0 throughout optimization. The fairness constraint term, C_{fair}, is assigned an adaptive penalty weight b, initially set to 1.0×10^{-6}. The fairness term can conflict with other geometric constraints, so b is deliberately set to a small value at the outset to prevent it from dominating the optimization. If b is too large, the resulting mesh becomes overly smooth (tending toward straightness), while too small a value can introduce undesirable distortions. As optimization proceeds, b vanishes to zero once the total objective function $F(\boldsymbol{X})$ reaches a threshold ϵ of 1.0×10^{-6}. This ensures that, at convergence, the final solution is governed solely by the primary geometric constraints, thereby avoiding unnecessary over-smoothing. This adaptive strategy for b was established through extensive testing to achieve an optimal accuracy of the mesh, while maintaining smoothness. The update schedule for b is predetermined and incorporated into the algorithm prior to optimization. Computational process and performance metrics, including the final cost $F_{min}=2.5 \times 10^{-15}$ and a total execution time of 15.0 s (Intel i9-10900H 2.80 GHz processor, Python implementation), are summarized in Fig. 4.

Upon convergence, the optimized vertex coordinates $\boldsymbol{v}_i$ are interpolated to reconstruct asymptotic polylines, yielding a refined and smooth asymptotic network. Fig. 5 depicts the resulting geometry, which is created using a comprehensive network of asymptotic curves. This optimized mesh is then converted into a NURBS (Non-Uniform Rational B-Splines) surface through interpolation. While this method enhances calculation accuracy—such that increasing the network density typically leads to more precise results—curvature analysis reveals some

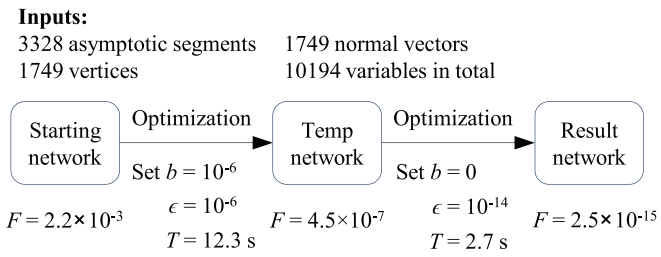

Fig. 4. Two-step optimization process for initial geometry design.

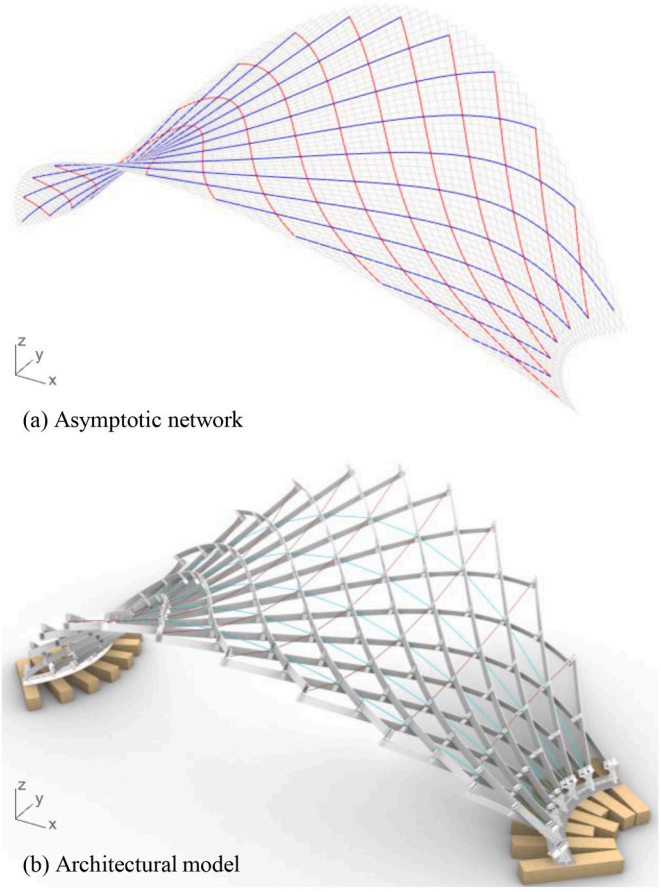

Fig. 5. Creation of Asymptotic Kinetic Canopy: (a) Optimized asymptotic network and NURBS surface; (b) Final architectural model.

limitations. Specifically, the optimized asymptotic curves achieve a maximum normal curvature of $\kappa_n = 0.0049\ m^{-1}$, which, while small, does not represent a strictly zero value. The residual non-zero normal curvature arises from the interpolation to NURBS. The observed value of $0.0049\ m^{-1}$ corresponds to a radius of curvature of approximately 204 m, which is well within production tolerance of the GFRP lamellas, making it negligible for architectural applications. Notably, the geodesic curvature remains comparatively high (maximum $\kappa_g = 0.6724\ m^{-1}$), underscoring the distinction between these two curvature measures.

For the architectural construction, a grid with less density is chosen, to lower material use, and cost, while ensuring structural stability. Only every fifth asymptotic curve is chosen to form an asymptotic plank. The grid is trimmed at the ground plane level to ensure all support joints are positioned at the same height. The final configuration comprises two sets of asymptotic curves (red/blue, 15 curves per set), achieving a maximum length of 5.87 m. Fig. 5b provides a detailed view of the architectural model, which spans 6 m. This model is employed for production and construction planning.

2.3. Service stages

The design geometry will be actuated to transform into various service stages. This transformation combines a rigid body mechanism via scissor hinges with the elastic deformation of asymptotic planks around their local weak axis, and thus facilitates a predictable, and controllable transformation. The structure's height and width are adjusted purely through the scissor movement of the grid, without changing the length of edges or adjusting the support point positions.

To simulate and quantify the kinetic behaviour, the continuous asymptotic network (Fig. 5a, red/blue) is discretized into polyline segments, forming a new model dedicated to transformation analysis (Fig. 6). In this discretized model, green points represent fixed supports, while a pink point denotes a designated control point used to parametrically adjust the transformation height.

In this model, we apply the *asym*ptotic constraint Eq. (1) and normalization constraint for normal vectors Eq. (2). Additionally, each segment-length of the asymptotic polylines is fixed using the following constraint formula:

$$C_{\text{asym\_leng}} = \sum_{i=1}^{N_{\text{asym}}} \left(\|\boldsymbol{v}_{ia} - \boldsymbol{v}_{ib}\|^2 - (l_{i-\text{initial}})^2 \right)^2 \tag{6}$$

where $l_{i-\text{initial}}$ is the initial length for each edge segment Edge i with its endpoints $\boldsymbol{v}_{ia}, \boldsymbol{v}_{ib}$ in the initial geometry.

We also fix the supports at their respective positions in the initial geometry using the constraint formula:

$$C_{\text{support}} = \sum_{i \in \text{support}} \|\boldsymbol{v}_i - \boldsymbol{v}_{i-\text{initial}}\|^2 \tag{7}$$

where $\boldsymbol{v}_{i-\text{initial}}$ is the target position for the support point $\boldsymbol{v}_i$.

To explore the various transformation stages, we control the height of the model's middle point. We introduce a new constraint term:

$$C_{\text{midpt}} = \|\boldsymbol{v}_{\text{midpt}} - \boldsymbol{v}_{\text{mid-target}}\|^2 \tag{8}$$

where $\boldsymbol{v}_{\text{mid-target}}$ is the target position for the middle point $\boldsymbol{v}_{\text{midpt}}$.

To sum above up, the transformation optimization is governed by the following nonlinear objective function:

$$F(\boldsymbol{X}) = C_{\text{A-net}}(\boldsymbol{X}) + C_{\text{norm}}(\boldsymbol{X}) + C_{\text{asym\_leng}}(\boldsymbol{X}) + C_{\text{support}}(\boldsymbol{X}) + C_{\text{midpt}}(\boldsymbol{X}) + bC_{\text{fair}}(\boldsymbol{X}) \tag{9}$$

where $\boldsymbol{X}$ represents the design variables (vertex coordinates and normal

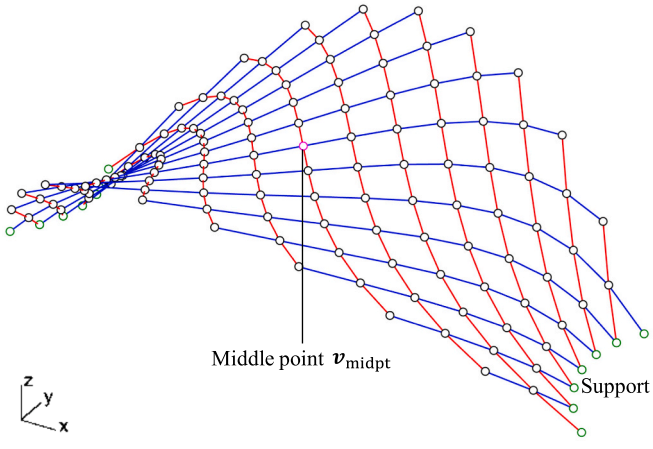

Fig. 6. Initialization of the kinetic canopy network for transformation optimization.

vectors).

This function builds upon the earlier formulation in Eq. (5), but is adapted for the transformation (simulation) stage rather than initial form-finding. While Eq. (5) is used to generate the geometry under prescribed boundary constraint C_{boundary}, Eq. (9) modifies the constraint set to reflect the requirements of transformation analysis. Specifically, the boundary constraint C_{boundary} is replaced by the support constraint C_{support}, which fixes the support locations to simulate realistic physical behaviour during transformation. Additionally, $C_{\text{asym\_leng}}$ is introduced to preserve the initial segment lengths of the asymptotic curves, and C_{midpt} is included to control and change the height of the model's midpoint, thus activating various service stages. The asymptotic constraints ($C_{\text{A-net}}$, C_{norm}) are retained to maintain the essential grid properties, while C_{fair} (with adaptive weight b) balances smoothness and accuracy.

In this function, all constraint terms are incorporated into the objective function via weights, following the approach detailed in Section 2.2. As illustrated in Fig. 7, the process begins with the initial design at Stage 4. Each subsequent stage (from 3 to 1 and from 5 to 6) of the asymptotic grid is generated by parametrically adjusting the mid-point elevation. At each subsequent generation the geometry from the previous stage serves as the starting point, and the objective function (including all constraint terms) is re-evaluated and optimized. This iterative approach ensures that the geometry evolves smoothly, allowing the constraints to guide the transformation toward the desired configuration. For each stage generation, the weights for $C_{\text{A-net}}$, C_{norm}, $C_{\text{asym\_leng}}$, C_{support} and C_{midpt} are fixed at 1.0 throughout the optimization process. As before, the fairness constraint C_{fair} is assigned an adaptive penalty weight b, initially set to 1.0×10^{-6} and finally adapted to 0 for each generation of stages 3 to 1. In the high-curvature geometries of the final two stages (5 and 6), the factor b was given a constant, higher value between 0.01 and 0.1 to promote smoothness. The transformation analysis provides foundational insights into the morphology of kinetic canopy networks; its exploratory nature necessitates rigorous validation using the nonlinear FE simulation detailed in Section 4.

According to the local coordinate system of the Darboux Frame, a comprehensive curvature analysis is conducted across multiple service stages of the canopy, as shown in Fig. 8. Throughout the transformation process, the network exhibits very low normal curvature. This consistency allows for the vertically arranged planks to be unrolled and produced from a flat, straight form. The structure capitalizes on the elastic deformation potential of the planks around their weak profile axis, while maintaining substantial bending stiffness around the local strong axis, thus ensuring a seamless transformation process. During the transformation, the geodesic curvature and geodesic torsion of each lamella within the structure undergo significant variations, which result in internal stress of the components. From Stage 1 to Stage 6, the geodesic curvature diminishes while the geodesic torsion increases. Naturally, due to gravitational forces, the grid will find its global equilibrium in a flat state (see Section 5). Consequently, it becomes imperative to devise specific actuation and locking strategies to control the desired geometry at different stages. These critical aspects will be discussed in detail in the subsequent sections.

3. Tectonic and construction development

With the computational design established, the following section will present the process going from geometry to construction, introducing the development for scissor joints, their fabrication planning, manufacturing, prefabrication and assembly, and actuation system.

3.1. GFRP plank and joint development

For elastic components, the most critical variables to consider are Young's modulus and permissible bending strength [32]. GFRP planks were selected as the primary building material due to their superior mechanical properties, particularly their exceptional ratio of strength to Young's modulus, which allows for greater achievable bending curvature and permissible twist. Based on the curvature analysis (Fig. 8) and Eqs. (10−12), a cross-section of 75 × 12 mm has been chosen to prevent any breakage resulting from geodesic curvature and geodesic torsion. Additionally, this cross-sectional dimension ensures sufficient structural capacity to support gravity loads and potential external forces.

As depicted in Fig. 5b, the dual sets of asymptotic planks are structured into two levels, linked by a vertical scissor joint. Fig. 9 is showing a close-up of this connection. This scissor joint, originally developed by Schikore [26], comprises two aluminum brackets connected by a central steel bolt, enabling rotational movement while maintaining structural integrity. Plastic washers are included to significantly reduce friction and facilitate smooth rotation. Sufficient space is maintained between the upper and lower planks to accommodate an actuation and stabilizing cable system.

The eccentric aluminum scissor joints introduce a fixed vertical offset of 46.5 mm and a horizontal offset of 18 mm between adjacent lamellas. This necessitates a specific layout principle for the planks and connecting bolts, illustrated in Fig. 10. While the actual asymptotic planks (red and blue) are positioned with a slight deviation from the theoretical asymptotic curves (dashed lines), the locations of the connecting bolts (purple) remain precisely aligned with the intersection nodes of the theoretical network. This ensures the kinematic integrity of the grid is maintained despite the physical offsets required for construction.

3.2. Prefabrication and assembly

The elastic deformation capacity of the grid is leveraged to significantly streamline the construction process. As illustrated in Fig. 11, two sets of planks are initially pre-fabricated with precisely positioned aluminum joints. These two sets of asymptotic planks are then assembled flat on the ground using steel bolts to form a two-tiered grid. In this flat state, the grid exhibits only geodesic curvature. The planar assembly is later transformed into a spatial, doubly curved structure by utilizing scissor hinges and exploiting the elastic bending (around the local z-axis) and twisting (around the local x-axis) of the GFRP lamellas.

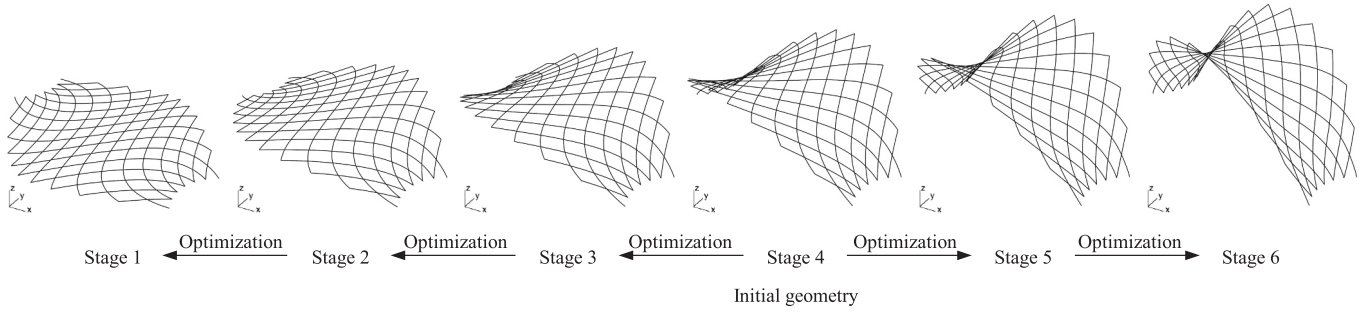

Fig. 7. Geometry generation for the kinetic canopy network at different service stages.

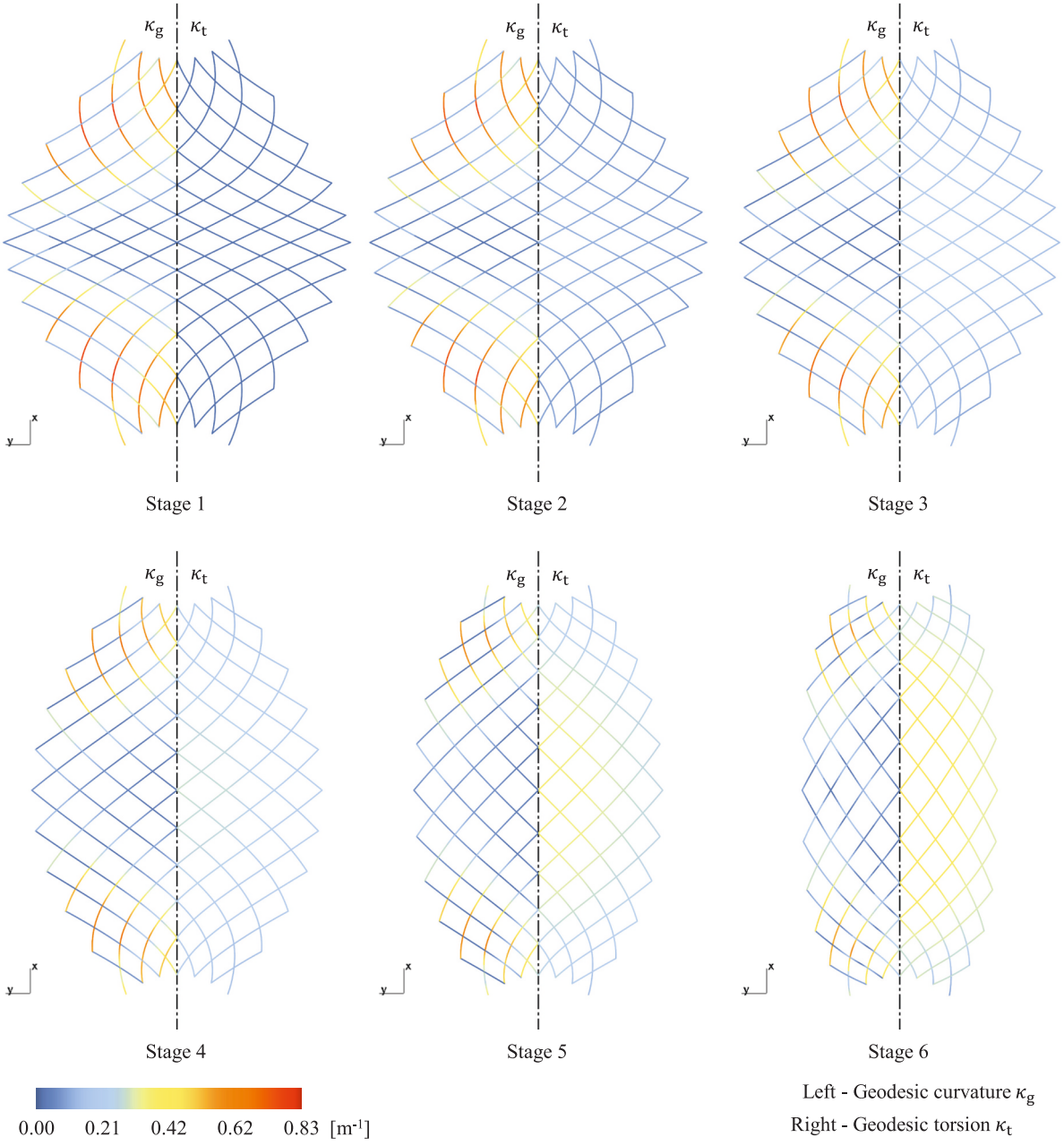

Fig. 8. Curvature analysis for the kinetic canopy network at different service stages.

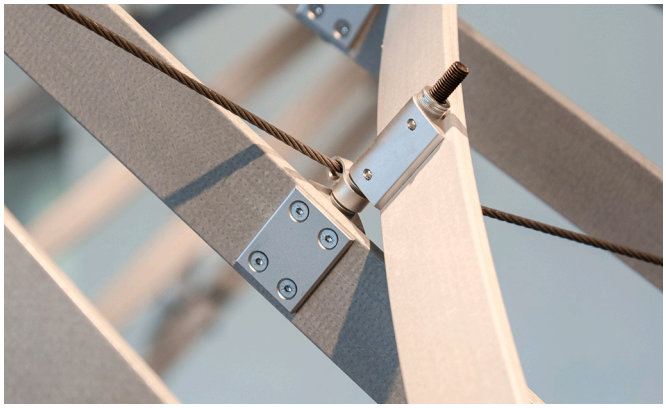

Fig. 9. Scissor joint connecting GFRP planks.

3.3. Support installation

In the conceptual design outlined in Section 2, we assumed that the 14 support nodes would be articulated as ideal ball joints, allowing unrestricted rotation in all directions. By studying their movement throughout stages 1–6, we can identify the active rotation axes: As shown in Fig. 12, a scissor-like rotation between asymptotic red and blue lines occurs within the grid and rotates freely around the normal direction ($\boldsymbol{n}_{B0}$) at the node (B). Furthermore, during transformation, the normal direction ($\boldsymbol{n}_{B1}$ & $\boldsymbol{n}_{B2}$) at the node (B) remains within this normal plane of the boundary edge (pink). In other words, the normal vector rotates around the tangent direction of the boundary edge at this node.

This movement informed the design of a specialized support configuration, shown in Fig. 13. The design incorporates a double-hinged mechanism: the asymptotic planks can rotate freely around the normal direction of the grid surface (bolt direction) to facilitate the scissor-like transformation, while a unidirectional hinge allows the

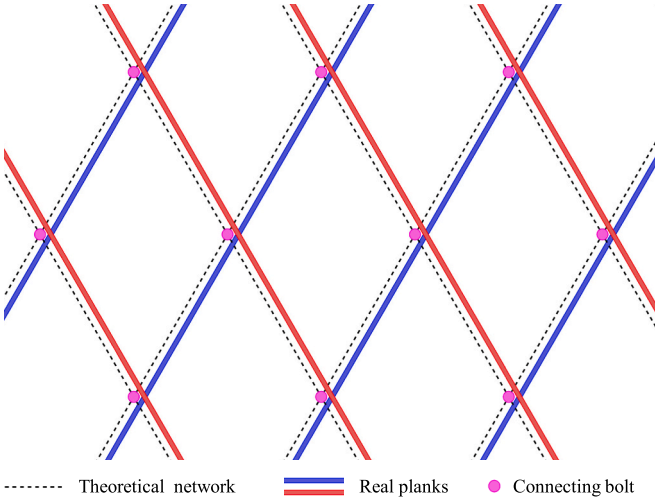

Fig. 10. Layout principle of asymptotic planks and bolts.

entire normal direction to rotate around an offset pin. This enables tilt at the ground contact points, permitting the vertical transformation of the entire structure. Compared to a conventional ball joint, this approach is simpler to construct and more effective in controlling the transformation. It does, however, create the horizontal and vertical hinge in slightly offset positions, which is carefully taken into account during kinetic simulation (see also Section 4.2). The supports were fabricated as two integrated structural units from laser-cut and welded 8 mm stainless steel plates.

As shown in Fig. 14a, the steel assemblies are mounted onto wooden elements with a 16 × 16 cm cross-section, providing flexibility for positioning actuation winches. To stabilize and anchor the system, the wooden supports rest on C-shaped steel profiles. Additionally, horizontal steel cables are installed as tension ties between opposing steel supports to enhance structural integrity.

3.4. Actuation system

To facilitate smooth transformation, we created an actuation system for the grid structure using steel cables, as depicted in Fig. 14. In alignment with the expected transformation pattern of our elastic grid structure, we strategically place a single, continuous cable along a serpentine route in the transverse directions of the structure. This cable

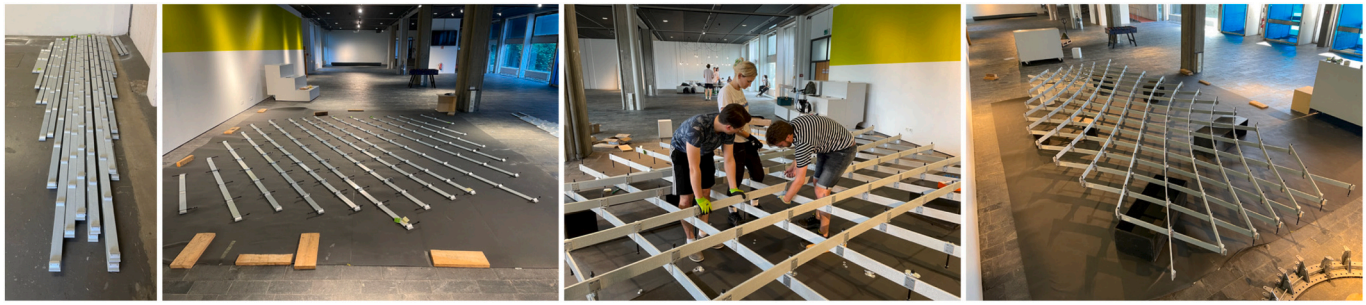

Fig. 11. Prefabrication and assembly process of planks.

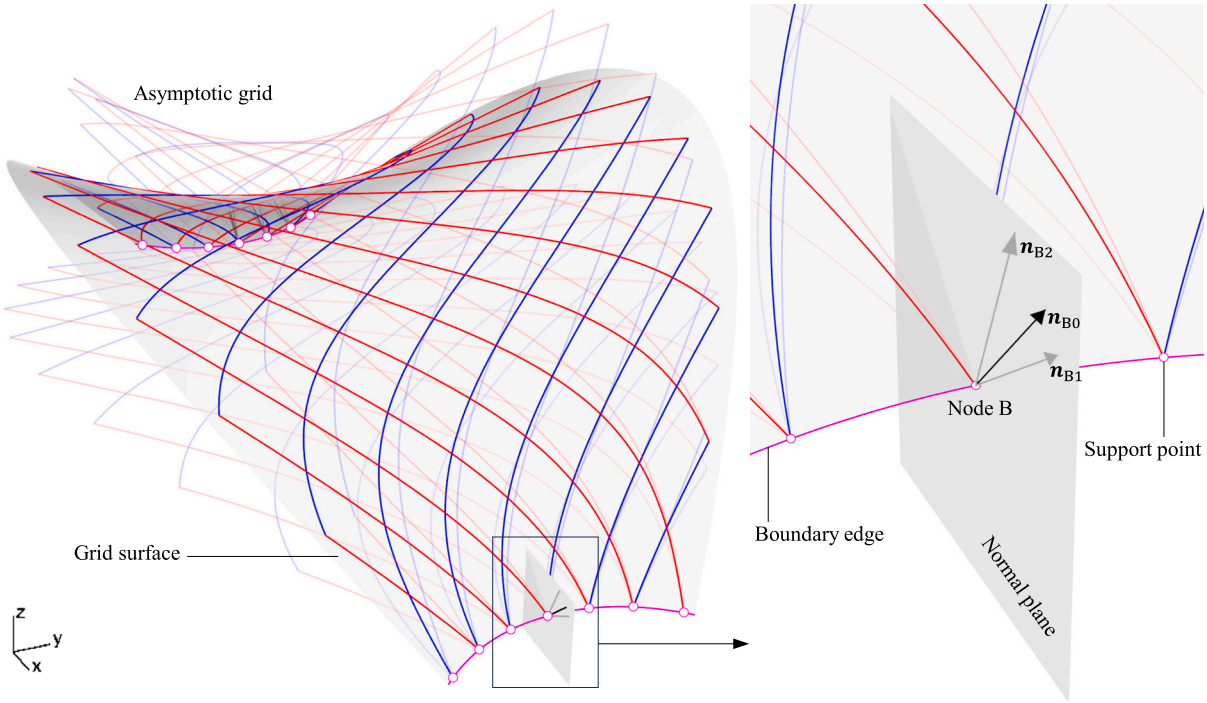

Fig. 12. Movement of support joint.

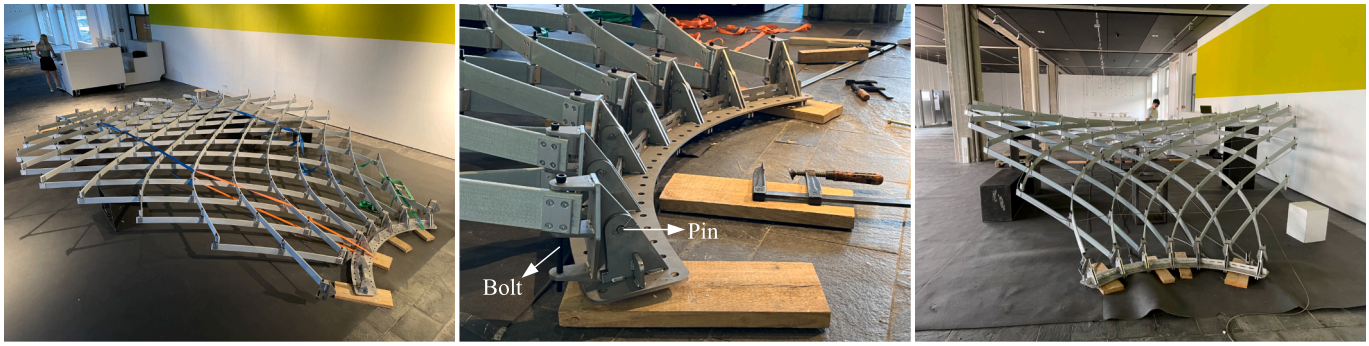

Fig. 13. Support installation and articulation conditions. Left: Installation process of the support system. Middle: Double-hinged support joints. Right: Vertical transformation via tilting at contact points.

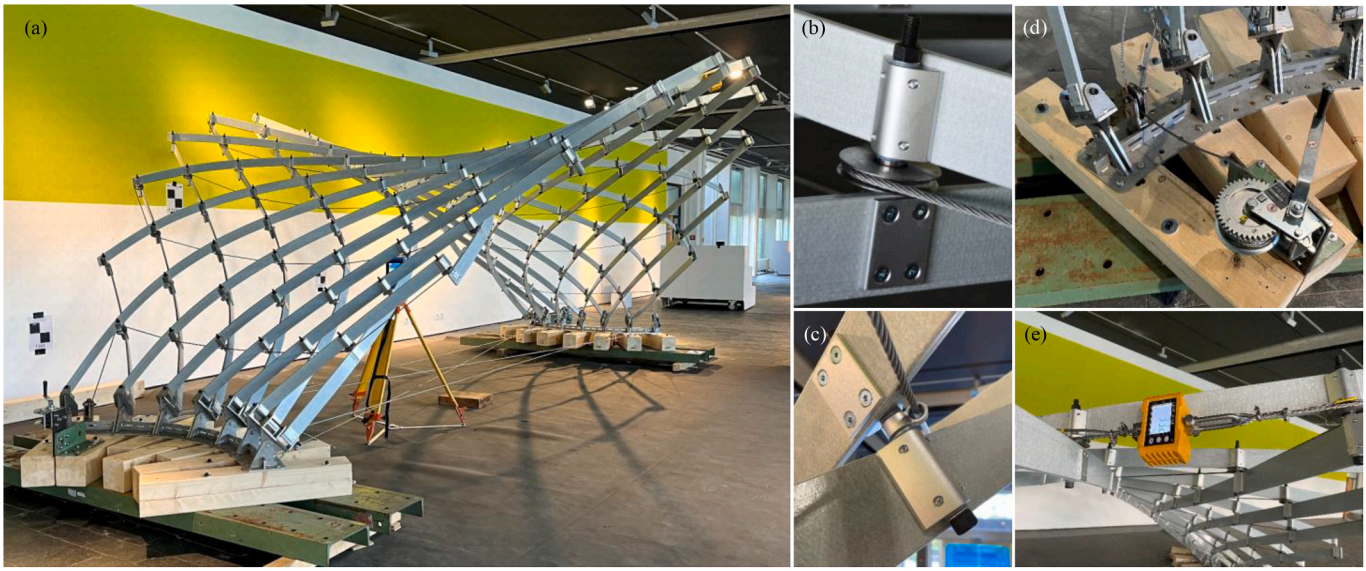

Fig. 14. Asymptotic Kinetic Canopy with actuation cable installed. (a) overall prototype; (b) Ball-bearing pulley joint; (c) sliding joint; (d) actuation winch and transition pulley; (e) tension sensor.

is a 6.0 mm diameter stainless steel rope with a 7 × 19 construction, providing high flexibility. It has a breaking load of approximately 1880 kg, ensuring both durability and effective actuation.

Fig. 14 shows the design layout for the actuation cable, which consists of two types of cable segments: the diagonal segments and the segments along the asymptotic planks. The diagonal cable creates a contraction of the quads, thereby altering the overall shape of the structure. To prevent excessive localized forces at the cable's turning points, we designed the cable route such that the change in direction at any node does not exceed 90 degrees, which we define as a "sharp angle" in this context. This criterion helps distribute forces more evenly and reduces localized stress concentrations along the cable.

To ensure smooth transformation, we designed two joints that connect the actuation cable to the assembled grid. As shown in Fig. 15, ball-bearing pulleys (b) were employed at corner nodes, while greased sliding joints (c) were designed for other nodes. At the supports, two additional transition pulleys (d) were arranged, allowing the actuation cable to adapt the direction from the grid to the winches during transformation. Two winches (d) were installed at the supports, enabling the extension or retraction of the actuation cable. A tension sensor (e) was strategically placed midway along the actuation cable to monitor tension levels accurately.

Lubricants were liberally applied to all nodal points and along the cable to reduce friction during actuation as much as possible. While these measures substantially lower friction, some residual effects

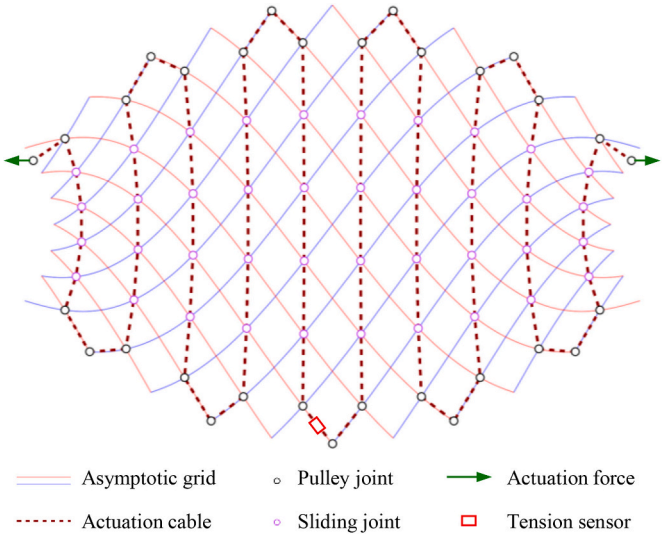

Fig. 15. Layout for actuation system.

remain, as analysed in detail in Section 5.2.

To ensure stability against wind and lateral forces in outdoor environments, stabilization cables were installed along the longitudinal direction of the structure after transformation. These cables are pretensioned and anchored at the support points, providing additional rigidity and allowing the structure to safely withstand environmental loads. Further details on this stabilization strategy are beyond the scope of this paper, which focuses on the transformation behaviour, and are thus not further discussed in the paper.

4. Finite element modelling

A Finite Element model was developed using Abaqus/Standard [33] to simulate the kinetic behaviour of the kinetic asymptotic prototype, incorporating large transformations via nonlinear simulation.

4.1. Asymptotic grid

The initial geometry (Fig. 5a) generated from the optimization process serves as the initial shape for constructing the FE model. Fig. 16 illustrates the support and hinge conditions, the coupling of nodes to simulate scissor connections, the Slip Ring connector for the actuation cable, and the corresponding pulling point. The planks are discretized using four-node shell elements with reduced integration (S4R). The model is simplified not accounting for the in-plane and out-of-plane eccentric effects of the planks. To simulate scissor connections, the three translational degrees of freedom at the nodes (orange), where the single-layer planks intersect, are directly coupled. This modelling approach avoids the need for additional strut connector elements significantly reducing modelling complexity and computational cost. Mesh convergence was established with an average element size of around 0.02 m (resulting in 24,128 S4R elements) by systematically evaluating element size (the most refined mesh considered had an element size of 0.01 m). This resolution accurately represents the curvature of each member and assures precision in the analysis.

The planks are composed of glass fibers embedded in an isophthalic polyester resin, with a glass fiber content ranging from 50 % to 65 %. The mechanical behaviour of the glass fiber-reinforced polymer (GFRP) material exhibits significant differences between axial and transversal directions, characterized by a relatively low shear modulus. This study utilizes a lamina material model within Abaqus to capture the orthotropic behaviour. Table 1 lists the material properties used in the FE model, which were provided by the supplier, FIBROLUX, and verified through initial material testing conducted as part of this study.

4.2. Boundary conditions

As discussed in Section 3.3, each structure support is designed as a unidirectional hinge support. During construction, the actual pivot point of the support and the intersection of the two sets of lamellas are offset by 105 mm, as illustrated in Fig. 16. To accurately simulate the rotational behaviour of the 14 support points, the study utilized the rigid body constraint in Abaqus. The actual pivot points of the structure were used as reference points (purple), which were then coupled with the ends of the corresponding lamellas (white) to form a rigid body. Each support point was defined to rotate solely around the *y*-axis of the corresponding local coordinate system. The translational degrees of freedom in the local *x*, *y*, and *z* directions and the rotational degrees of freedom around the local *x* and *z* axes were constrained. Additionally, the nodes (white) at the corresponding lamella end positions were restricted within the *xz* plane of the corresponding local coordinate system. Through these settings, the boundary conditions of the actual model can be realistically simulated.

4.3. Pulley system

Fig. 16 shows the utilization of a Slip Ring connector to simulate the actuation pulley system. The connector is a long, continuous polygon edge that links the actuation joints. During the transformation process, the overall length of the cable remains constant, while the cable is able to slide freely at the intermediate joints, allowing individual segment lengths to adjust as needed. Actuation of the structure is accomplished by pulling the designated pulling point (indicated in red). In this model, friction between the cable and the joints is not considered; as a result, the tension (traction) in the cable is uniform along its entire length at all stages of the transformation. The simulation enables the documentation of cable forces throughout the transformation process, allowing for direct comparison with experimental data. To accurately represent the real structure, a direction-conversion pulley is included and modelled in its correct position (indicated in yellow).

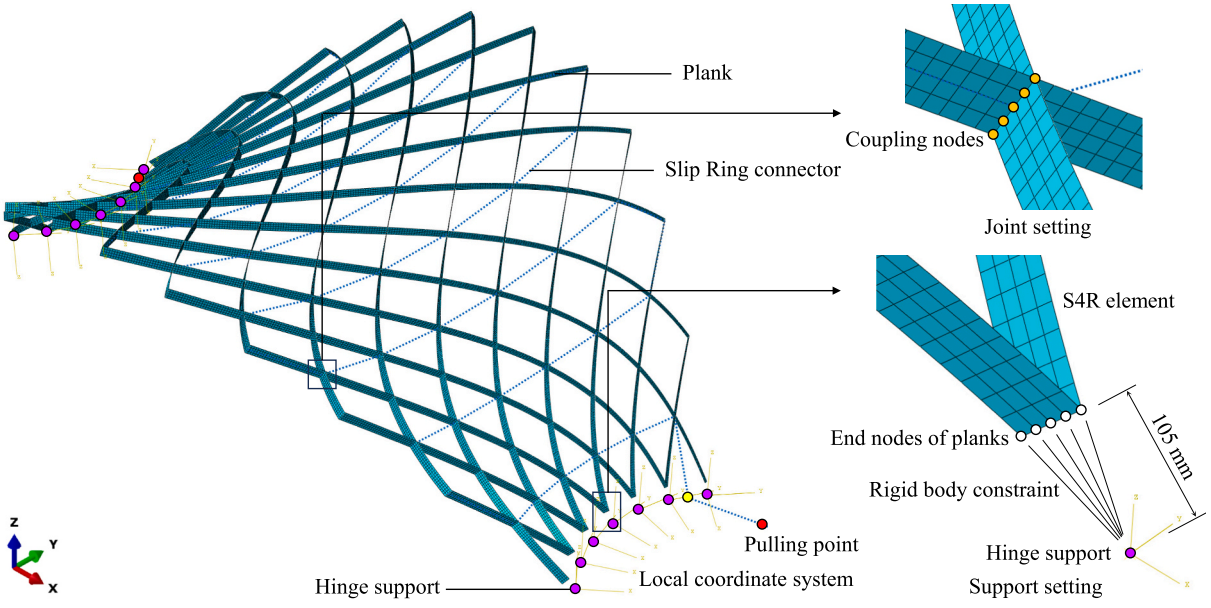

Fig. 16. Finite element model of the asymptotic kinetic canopy.

Table 1
Material properties of steel and GFRP used in the FEM model.

Material	Elastic modulus E (N/mm^2)	Shear modulus G (N/mm^2)	Poisson's ratio ν	Density ρ (kg/m^3)	Yield/breaking strength f_y (N/mm^2)	Shear strength τ_y (N/mm^2)
GFRP	$E_1 = 2.8 \times 10^4$ (axial) $E_2 = 9.5 \times 10^3$ (transversal)	3.0×10^3	0.3	2075	250	30

4.4. Initial stress

The construction process of the kinetic canopy introduces initial stresses into the GFRP planks through elastic bending and twisting, as the planks are transformed from their original straight state into the designed curved configuration. These internal stresses are present in the structure immediately after assembly—prior to any external actuation or loading—and result directly from the manufacturing and assembly procedures.

Within nonlinear FEM, the initial stress of the as-built geometry (Fig. 5a) incurred during the construction process is determined through a "*flatten and reduction*" method [17]. This approach contrasts with the traditional simulation method that transitions from a flat shape to its deformed configuration [34]. This technique allows for the inclusion of various forms of initial stress in the shell-element model, including the bending stress resulting from bending curvature, the shear stress from torsion, and the axial stress due to the Helix-Torsion effect [24,35]. The distribution of these initial stresses directly reflects the curvature values obtained in the curvature analysis presented in Fig. 8 (Stage 4). Based on the local coordinate system (Fig. 1), the Euler-Bernoulli bending stress σ_{max}, Saint-Venant shear stress τ_{max} and additional normal stress σ_H due to Helix-Torsion effect can be computed as follows:

$$\sigma_{max} = \frac{E_1 t \kappa_g}{2} \tag{10}$$

$$\tau_{max} = \frac{G I_T \kappa_t}{W_T} \tag{11}$$

$$\sigma_H = \frac{1}{2} E_1 \left(r^2 - i_p^2\right) \kappa_t^2 \tag{12}$$

where E_1 is Young's modulus in the axial direction, G is the shear modulus, t is the lamella thickness, I_T is the torsional moment of inertia, W_T is the section modulus, r is the distance between the monitoring point and the centre in the cross-section of the lamella, and i_p the polar radius of gyration.

4.5. Simulation scheme

The FE simulations were conducted in two main phases, the initial balanced equilibrium state (1), and the actuation induced transformation (2), to accurately replicate the transformation process and structural behaviour of the prototype.

4.5.1. Phase 1: initial balanced equilibrium state

In the first step, both the initial stresses (as described above) and gravity loads were applied to the FE model, which was configured according to the initial design geometry (Fig. 5a). The gravity load accounted for the self-weight of the GFRP planks (totalling 225.28 kg), as well as the additional weights of 0.81 kg and 0.56 kg assigned to the pulley joints and rest joints, respectively.

All loads were applied simultaneously, and the structure was allowed to reach a new equilibrium state via a nonlinear solution step. During this process, both ends of the actuation cable were fixed, with the total cable length held constant, modelling the cable as inextensible. However, the cable was allowed to slide freely at all intermediate joints, enabling individual segment lengths to adjust in response to structural deformation. Importantly, no explicit cable pre-loads were prescribed; the resulting cable force emerged naturally as part of the equilibrium solution. This simulation approach captures the redistribution of internal stresses and accounts for the deformability of the structure, as the nonlinear FE solver iteratively satisfies both the imposed initial stresses and the equilibrium conditions.

As an outcome of this phase, the total horizontal thrust at one side of the arch-like canopy was calculated to be approximately 1.401 kN in the global x-direction. The resulting axial stress distribution along the planks is presented in Fig. 17, with tension observed on the exterior side of the bent planks and compression on the interior side—indicating that bending stress predominates. The maximum deformation from the intended design shape (Fig. 5a) was found to be only 12 mm at the side edges, demonstrating that the equilibrium configuration remains very close to the target geometry. This balanced equilibrium state (corresponding to Stage 4 in Fig. 7) is used as the starting point for subsequent transformation analyses.

4.5.2. Phase 2: actuation-induced transformation

Building on this equilibrium state, and keeping all other model settings unchanged, the second phase involves applying a controlled displacement to one end of the actuation cable (red point in Fig. 16). By tightening or loosening the cable at this point, geometric transformation of the entire structure is induced, simulating the actual actuation process observed in the experiments.

5. Results and discussion

Upon completion of the prototype, transformation experiments were conducted to observe and validate the structure's transformation capacity, to understand the control of the driving cable.

5.1. Transformation process

The transformation process was implemented using the installed actuation system, deploying the structure from Stage 1 (flat) to Stage 6 (with a rise of 2.625 m), as depicted in Fig. 18. Stage 4 represents the initial design geometry. Both winches at the supports were rotated synchronously at equal speeds, allowing precise control over the height

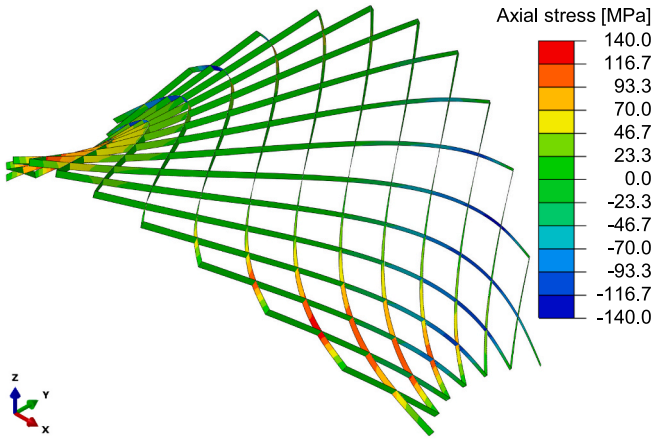

Fig. 17. Result axial stress of the asymptotic kinetic canopy based on the initial geometry (Stage 4).

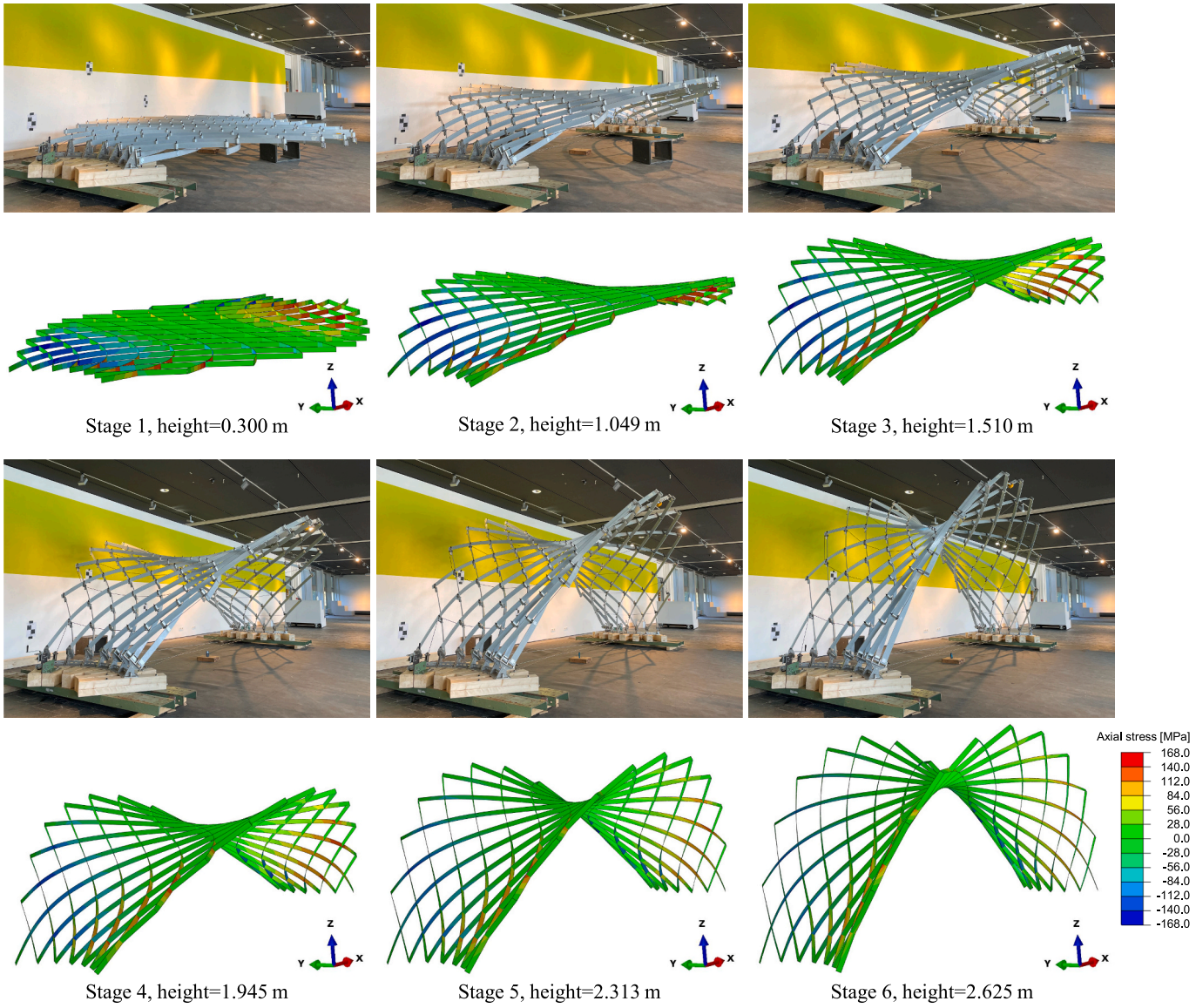

Fig. 18. Transformation process actuated by the winch cable. Top: physical model; bottom: FE model.

of the central point. In this way, the tension sensor (see Fig. 14e) was kept within the original grid to prevent interference with adjacent joints. The winch-actuation facilitated a smooth transformation of the grid in the intended direction, which was captured at various operational stages.

For the FE simulation, the analysis began from the balanced equilibrium configuration (Stage 4 in Fig. 7), which accounts for the initial pre-stress and self-weight, see Section 4.5. In the transformation simulation, one end of the actuation cable was fixed, while the other end (red point in Fig. 16) was manipulated to control the transformation. By precisely specifying the amount of cable displacement—either by pulling for upward transformation (Stages 5 & 6) or loosening for downward transformation (Stages 1–3)—the structure's response was captured through a series of nonlinear analyses.

This modelling approach provided quantitative agreement in central height and qualitative agreement in overall configuration between the experimental results and the FE predictions across all stages (1–6). From the FE simulation results, the axial stress distributions at each stage were extracted and analysed, as shown in Fig. 18. The bending stress within the structural components gradually decreased from Stage 1 to Stage 6, while the torsional stress increased as the structure transformed. Throughout the entire transformation process, the maximum bending stress (168 MPa) and shear stress (18 MPa) remained within the elastic limits of the material, confirming the structural safety and reliability of the transformation mechanism.

5.2. *Actuation force*

The prototype enables structural transformation through manually controlled actuation. Fig. 19 illustrates the relationship between the midpoint cable force (measured via the tension sensor in Fig. 14e) and the central elevation. During transformation, the actuation cable force decreases as the height increases to 1.945 m (Stage 5), driven by the growing curvature of the grid that redistributes stresses. Beyond this threshold, the force reverses trend and rises due to accumulating elastic bending and torsional stresses in the planks. Notably, the fully flat configuration represents a theoretical singularity: infinite actuation force is required to initiate motion from this symmetric state, as directional transformation bias vanishes. To circumvent this, practical transformation requires either (1) a mechanical system to lift the central grid slightly from the flat state before engaging cable actuation, or (2) exclusion of the flat configuration entirely in the kinetic workflow,

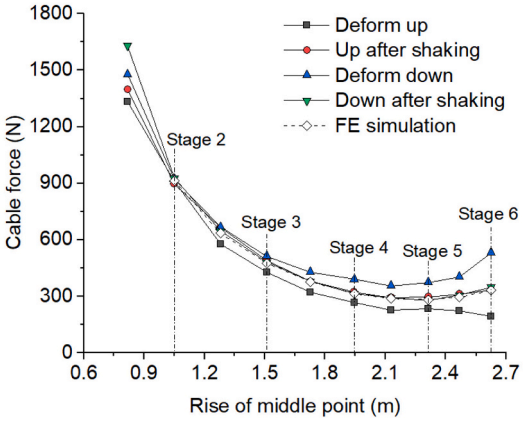

Fig. 19. Cable force monitored with (black and blue), and without (red and green) friction-effects during transformation. (For interpretation of the references to colour in this figure legend, the reader is referred to the web version of this article.)

ensuring the centre of the structure remains in a predefined elevation range post-construction.

In our experiment, the cable forces are measured at the highest point in the centre of the actuation cable. Under ideal conditions without friction, the internal forces within a continuous cable (with negligible self-weight) should be uniformly distributed. However, it should be noted that the cable forces recorded are larger during downward transformations and lower during upward transformations (Fig. 19). The observed inconsistency in cable tension arises from friction's directional dependence during actuation. During upward transformation, pulling the cable results in an uneven tightening: the friction between the cable and scissor joints acts as a resistance to motion, thereby causing a concentration of tension near the winches. This is similar to the tightening of a shoelace where the initial force is localized at the pulled ends. As a result, the gravity of the structure is primarily carried by the cables near the supports, while the internal force measured in the central pull cable (at the tension sensor) is significantly reduced and appears relatively small. On the other hand, during downward transformation, friction hinders the cable segments to slide from the supports to the centre region, resulting in a slower release of the cable segments in the centre region. The abrupt loosening of the cable significantly decreases tension near the winches; hence, the weight of the structure is mainly borne by the central part of the actuation cable, showing high tension on the sensor.

To assess the effect of friction in more detail, we conducted two tests involving upward and downward transformation. In each test, we deformed the structure up or down to achieve a specific shape or height and recorded the readings of the tension sensor. We then shook the structure to help the cable shift and eliminate any friction effect, then recorded the readings of the tension sensor again. After the shaking, the effect of friction was completely released, and the internal force across the length of the actuation cable approximated uniformity. In the upward transformation experiment, the actuation effect was homogenously distributed to the central region, thus increasing the cable tension at the centre compared to before the shake. In the downward transformation test, the loosening effect was distributed to the central region, and the cable tension at the centre decreased compared to before the shake. These observations have been confirmed in the test results shown in Fig. 19. Moreover, under identical shape or height conditions, the readings of the tension sensor for the two scenarios (upward post-shaking, and downward post-shaking) were strikingly similar. These findings align closely with frictionless FE simulations, showing within 2 % deviation for Stages 2–5 and within 5 % at Stage 6. In the absence of any friction within the prototype, only approximately 915 N and 280 N are required to actuate and secure the structure for Stage 2 and Stage 5, respectively.

However, due to the conditions of the experiment, the actual actuation forces at the winches were not recorded. In practice, these forces are higher than the results documented post-shaking during the upward transformation process, and conversely lower during the downward transformation process.

5.3. Energy variation

Based on the FE simulation that disregards friction effects, Fig. 20 delineates the relationship between the actuation cable's loose/traction length and the force required during the transformation process. As the actuation cable's length diminishes, the diagonal length of each grid unit in the central area progressively reduces in the transverse direction while increasing in the longitudinal direction. Consequently, the entire structure's height gradually increases, while the width of the span diminishes. During upward transformation, the cable's tensioning speed variably impacts the structure's height. Initially, the alteration in cable length significantly influences the rise reconfiguration, and this influence gradually lessens with continued actuation, as indicated by the varying widths of Processes A, B, C, and D. These processes represent the four consecutive transformation courses from Stage 2 to Stage 6.

The energy input required by the actuation cable during structural transformation can be evaluated using the work-energy principle. For example, when the structure transitions from State 3 to State 4, the work performed by the actuation cable is given by:

$$W = \int_a^b Force(x)dx \tag{13}$$

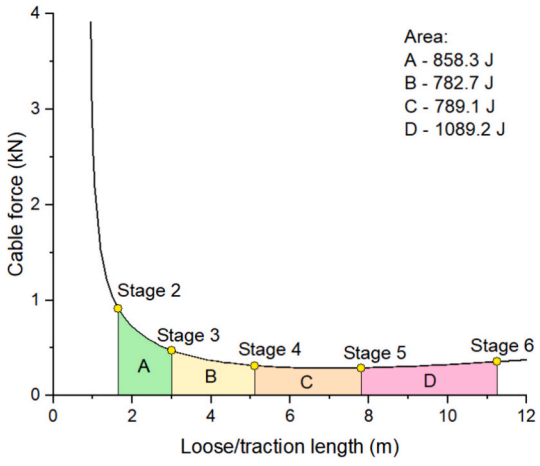

Fig. 20. Evolution of cable force as a function of the actuation cable's loosening and traction length during the transformation process.

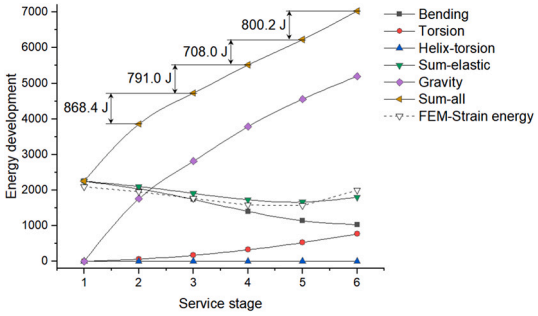

Fig. 21. Energy development during transformation based on the curvature analysis and FE simulation.

where *Force*(*x*) is the driving force in the cable corresponding to the traction length *x*, and *a* and *b* are the traction lengths corresponding to States 3 and 4, respectively. This equation does not account for friction effects.

According to Eq. (13), Fig. 20, the filled area between the curve and the baseline represents the energy required to transition the structure between specific stages. For instance, Area B, equivalent to 782.7 J, denotes the minimal energy necessary to actuate the structure from Stage 3 to Stage 4.

During the process of upward transformation, the fluctuations in energy primarily originate from two key components: elastic strain energy Π_e and gravitational potential energy Π_g.

The elastic strain energy, which is stored within the system's GFRP planks, is subdivided into three major components: bending (Π_{bending}), torsion (Π_{torsion}), and helix-torsion ($\Pi_{\text{Helix-Torsion}}$) [24,35]. These can be calculated based on the geodesic curvature κ_g, and the geodesic torsion κ_t. At every stage of the transformation process, the elastic strain energy can be expressed as follow:

$$\Pi_e = \Pi_{\text{bending}} + \Pi_{\text{torsion}} + \Pi_{\text{Helix-Torsion}}$$

$$= \frac{1}{2}E_1 I_y \int \kappa_g^2 ds + \frac{1}{2}GI_T \int \kappa_t^2 ds + \frac{1}{18}E_1 I_r \int \kappa_t^4 ds \tag{14}$$

where I_r is the helix area moment of the cross-section:

$$I_r = \int r^4 dA \tag{15}$$

where A is the cross-section area, r is the distance between the monitoring point and the centre in the cross-section of the lamella.

The gravitational potential energy consists of two components: GFRP planks $\Pi_{g,\text{GFRP}}$, and joint weights $\Pi_{g,\text{joint}}$. The gravitational potential energy can be expressed:

$$\Pi_g = \Pi_{g,\text{GFRP}} + \Pi_{g,\text{joint}} = \rho g A \int H ds + \sum_{i \in \text{joint}} m_i g h_i \tag{16}$$

where ρ is the density of GFRP, g is the gravitational acceleration, H is the height of measuring point ds to the ground, m_i is the sum mass of the aluminum and steel for joint i, and h_i is the height of the joint i to the ground.

Figure 21 depicts the energy progression of the entire structure during the transformation process, as analysed through curvature analysis (Fig. 8) and Eqs. (14 and 16). From Stage 1 to Stage 6, there was a noticeable decrease in bending energy accompanied by an increase in torsion energy, with the energy associated with helix-torsion remaining insignificant. The strain energy results obtained from FE simulations are compared with analytical calculations for verification. Theoretically, the strain energy derived from FE simulation should align with the cumulative elastic energy from bending (Π_{bending}), torsion (Π_{torsion}), and helix-torsion ($\Pi_{\text{Helix-Torsion}}$) as per the curvature analysis. The comparative outcomes indicate a maximum variance of ±8.9 % between the two calculation methods for Stages 4 and 6, suggesting a general consistency in the energy trends observed in both approaches. At Stage 5, the structure exhibited minimal elastic energy, indicative of a self-equilibrium state in the absence of external forces such as gravity.

Table 2
Energy required to change the stages, comparing curvature analysis and FE-simulation based on Fig. 20 and Fig. 21.

Process	Process A (Stages 2 – 3)	Process B (Stages 3 – 4)	Process C (Stages 4 – 5)	Process D (Stages 5 – 6)
Length variation (m)	1.35	2.10	2.70	3.45
Height variation (m)	0.461	0.435	0.368	0.312
Curvature analysis (J)	868.4	791.0	708.0	800.2
FE Model (J)	858.3	782.7	789.1	1089.2
Difference (%)	1.2	1.1	−10.3	−26.5

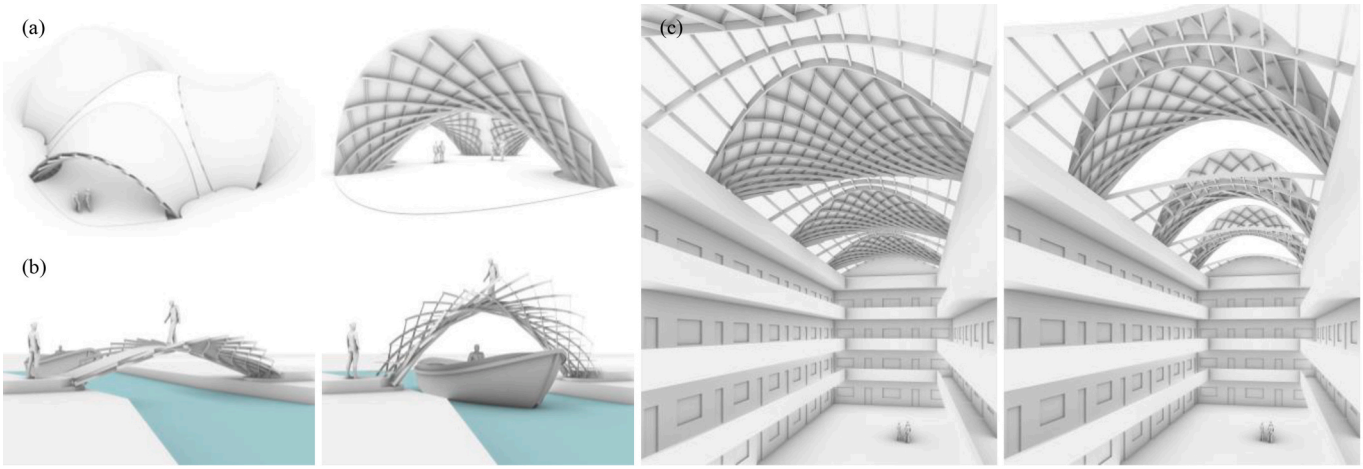

Fig. 22. Architectural application scenarios. (a) Temporary Event Canopy; (b) Kinetic Bridge; (c) Kinetic Roof.

Nonetheless, the predominant energy stored in the structure was gravitational potential energy, necessitating the input of additional energy to facilitate an upward transformation of the structure.

Table 2 illustrates the necessary adjustments in the length of the actuation cable, either by extension or contraction, and evaluates the energy demands associated with these changes across sequential stages. The energy variations calculated from curvature analysis (as shown in Fig. 21) are in close agreement with the frictionless FE simulation data (Fig. 20) for Processes A and B, with minor discrepancies of −1.2 % and − 1.1 %, respectively. However, the deviation increases significantly to +26.5 % between Stage 5 and Stage 6. This increase is attributed to the complex doubly curved surface encountered in higher stages, where the stress distribution among the elastic components becomes more complex and deviates from the expected curvatures, as detailed in the stress distribution analysis for Stages 5 and 6 presented in Fig. 18. Consequently, additional energy is required to attain equilibrium at these stages.

The analysis of cable force, in relation to traction length, structural height and energy development offers to evaluate and separate precisely the internal constraints at play in this kinetic transformation.

5.4. Application scenarios

The innovative use of kinetic asymptotic structures promises benefits across architectural and engineering applications. Fig. 22 outlines three exemplary use cases for this technology: a temporary event canopy (a), a kinetic bridge (b), and an adaptive roof (c). The canopy, when not in use, can be flattened and hidden beneath the floor and elevated to provide shelter when needed. The bridge can remain low in its standard stage but can be raised to allow boat passage when necessary. The kinetic roof, typically maintained in a flattened stage, can be adjusted to a higher position to enhance natural light or air circulation when required.

6. Conclusion and outlook

This paper presented a computational framework, with an emphasis on experimental construction and actuation strategies, for developing kinetic transformable structures based on elastic asymptotic networks. By integrating elastic asymptotic planks with standard scissor joints, we facilitate predictable, smooth transformations. The approach was demonstrated through the design, simulation, and physical realization of the Kinetic Canopy—a 6 m-span prototype constructed from flat GFRP planks. Key innovations include a manually operated cable-pulley actuation system enabling precise dual-winch control and a modular assembly process.

A frictionless, single-layer simplified non-linear FE model was used to evaluate the system's kinetic performance, providing reasonable estimates of stress distributions, actuation forces, and transformation paths. Experimental validation revealed strong agreement between simulated and measured cable forces, affirming the fidelity of the simulation approach. However, experimental validation revealed that, despite significant efforts to minimize friction—such as the use of plastic washers at joints, flexible cables, lubricants, and a carefully designed pulley system—residual friction was still present in the prototype. This residual friction, although minor, contributed to discrepancies between simulated and measured actuation forces. Importantly, these friction-reducing strategies were sufficient to ensure smooth, reliable transformations, and allowed for manual operation of the winch system with relatively low force. Thus, while friction does not dominate the system's behaviour, it remains a non-negligible factor in practical applications.

Energy component analysis highlighted gravitational forces as the primary resistance during upward motion, with elastic strain energy playing a negligible role. The curvature-based energy model exhibited exceptional alignment with FE results in early transformation phases, validating the geometric design framework. Practical advantages such as low operational forces for manual control and modular scalability position this system as adaptable to diverse applications, including event canopies, bridges, or deployable roofs.

Future research will pursue two directions: 1) design and construction of a kinetic facade prototype for high-rise buildings, exploring different actuation methods to enhance the applicability of such structures across diverse architectural scenarios; and 2) advances in actuation and stabilization, particularly the development of motorized actuation mechanisms and intelligent stabilization strategies to increase load-bearing capacity and enable real-time adaptive responses to environmental factors such as wind and sunlight. Key practical challenges include addressing singularities—such as complete structural flattening in the Kinetic Canopy prototype—and integrating real-time structural health monitoring systems to detect and prevent misactuation or potential damage.

Supplementary data to this article can be found online at https://doi.org/10.1016/j.autcon.2025.106508.

CRediT authorship contribution statement

Zongshuai Wan: Writing – review & editing, Writing – original draft, Visualization, Validation, Software, Resources, Project administration, Methodology, Investigation, Funding acquisition, Formal analysis, Data curation, Conceptualization. **Haotian Man:** Visualization, Investigation. **Kristof Crolla:** Writing – review & editing, Resources, Project administration, Funding acquisition. **Eike Schling:** Writing – review & editing, Visualization, Validation, Supervision, Resources, Project administration, Investigation, Funding acquisition, Conceptualization.

Declaration of competing interest

The authors declare that they have no known competing financial interests or personal relationships that could have appeared to influence the work reported in this paper.

Acknowledgements

We gratefully acknowledge the financial support that has made this research possible, provided by the Research Grants Council of Hong Kong through the General Research Fund (Grant No. 17607023) and the National Natural Science Foundation of China (Grant No. 52308208). We would also like to extend special appreciation to Dr. Jonas Schikore for his invaluable guidance and insightful feedback on the design. We thank Chau Ching Ho Marco, Ruoyi Chen, Yim Yung Ching, Gaby Davina Lendy, and Lin Yu at HKU for their assistance during the design phase. We thank Tim Riechers, Paulina Kirschke, Marie Engelking, and Christian Reck for their effort in prefabricating, construction and transformation testing of the prototype. We are also thankful to FIBROLUX and ALPAKA for their contributions to producing the GFRP planks and steel supports, which were critical to the success of our project.

Data availability

Data will be made available on request.

References

[1] W. Zuk, R.H. Clark, Kinetic Architecture, Van Nostrand Reinhold Company, New York, 1970.
[2] A. Tabadkani, A. Roetzel, H.X. Li, A. Tsangrassoulis, A review of occupant-centric control strategies for adaptive facades, Autom. Constr. 122 (2021), https://doi.org/10.1016/j.autcon.2020.103464.
[3] J. Böke, U. Knaack, M. Hemmerling, Automated adaptive façade functions in practice - case studies on office buildings, Autom. Constr. 113 (2020), https://doi.org/10.1016/j.autcon.2020.103113.
[4] A. Tabadkani, A. Roetzel, H.X. Li, A. Tsangrassoulis, Design approaches and typologies of adaptive facades: a review, Autom. Constr. 121 (2021), https://doi.org/10.1016/j.autcon.2020.103450.

[5] S. Schleicher, Bio-inspired compliant mechanisms for architectural design: transferring bending and folding principles of plant leaves to flexible kinetic structures, Univer. Stuttgart (2016), https://doi.org/10.18419/opus-123.
[6] E. Soriano, Low-tech geodesic gridshell: almond pavilion, ArchiDOCT 4 (2017).
[7] J. Panetta, M. Konaković-Luković, F. Isvoranu, E. Bouleau, M. Pauly, X-shells: a new class of deployable beam structures, ACM Trans. Graph. 38 (2019), https://doi.org/10.1145/3306346.3323040.
[8] M. Bi, Y. He, Z. Li, T.U. Lee, Y.M. Xie, Design and construction of kinetic structures based on elastica strips, Autom. Constr. 146 (2023), https://doi.org/10.1016/j.autcon.2022.104659.
[9] X. Tellier, Bundling elastic gridshells with alignable nets. Part I: analytical approach, Autom. Constr. 141 (2022), https://doi.org/10.1016/j.autcon.2022.104291.
[10] X. Tellier, Bundling Elastic Gridshells with Alignable Nets. Part II: Form-finding, Autom Constr, 2022, p. 141, https://doi.org/10.1016/j.autcon.2022.104292.
[11] D. Pellis, Alignable Lamella Gridshells, ACM Trans. Graph. 43 (2024) 1–21, https://doi.org/10.1145/3687898.
[12] H. Pottmann, A. Asperl, M. Hofer, M. Kilian, Architectural Geometry, Bentley Institute Press, 2007. https://repositum.tuwien.at/handle/20.500.12708/22181 (accessed September 11, 2023).
[13] C. Tang, M. Kilian, P. Bo, J. Wallner, H. Pottmann, Analysis and design of curved support structures, in: Advances in Architectural Geometry 2016, vdf Hochschulverlag AG an der ETH Zürich, Zürich, 2016, pp. 9–23, https://doi.org/10.3218/3778-4_4.
[14] E. Schling, Repetitive structures: design and construction of curved support structures with repetitive parameters, Tech. Univer. Munich (2018), https://doi.org/10.14459/2018md1449869.
[15] E. Schling, D. Hitrec, J. Schikore, R. Barthel, Design and construction of the asymptotic pavilion, in: Eugenio Onate, Kai-Uwe Bletzinger, Bernd Kroplin (Eds.), 8th International Conference on Textile Composites and Inflatable Structures - STRUCTURAL MEMBRANES 2017, International Center for Numerical Methods in Engineering, Munich, 2018, pp. 178–189. https://mediatum.ub.tum.de/doc/1468899/1468899.pdf.
[16] J. Schikore, E. Schling, T. Oberbichler, A.M. Bauer, Kinetics and design of semi-compliant grid mechanisms, in: Olivier Baverel, Helmut Pottmann, Caitlin Mueller, Tomohiro Tachi (Eds.), Advances in Architectural Geometry AAG 2020, Paris, 2021, pp. 108–129. https://thinkshell.fr/wp-content/uploads/2019/10/AAG2020_06_Schikore.pdf (accessed August 25, 2025).
[17] E. Schling, Z. Wan, A geometry-based design approach and structural behaviour for an asymptotic curtain wall system, J. Build. Eng. 52 (2022), https://doi.org/10.1016/j.jobe.2022.104432.
[18] Z. Wan, E. Schling, Structural principles of an asymptotic lamella curtain wall, Thin-Walled Struct. 180 (2022), https://doi.org/10.1016/j.tws.2022.109772.
[19] Z. Wan, E. Schling, Structural behaviour of an asymptotic curtain wall stiffened with lamella couplings, J. Constr. Steel Res. 207 (2023) 107938, https://doi.org/10.1016/j.jcsr.2023.107938.
[20] E. Schling, Z. Wan, H. Wang, P. D'Acunto, Asymptotic geodesic hybrid timber Gridshell, in: Advances in Architectural Geometry 2023, De Gruyter, 2023, pp. 97–110, https://doi.org/10.1515/9783111162683-008.
[21] Z. Wan, P. D'Acunto, E. Schling, Structural behaviour of asymptotic geodesic hybrid timber gridshells, Eng. Struct. 308 (2024) 117918, https://doi.org/10.1016/j.engstruct.2024.117918.
[22] B. Wang, M. Almaskin, H. Pottmann, Computational design of asymptotic geodesic hybrid gridshells via propagation algorithms, Comput. Aided Des. 178 (2025) 103800, https://doi.org/10.1016/j.cad.2024.103800.
[23] J.A. Cottrell, T.J.R. Hughes, Y. Bazilevs, Isogeometric Analysis: Toward Integration of CAD and FEA, 2009, https://doi.org/10.1002/9780470749081.
[24] J. Schikore, A.M. Bauer, R. Barthel, K.U. Bletzinger, Large torsion on elastic lamella grid structures, in: Carlos Lazaro, Kai-Uwe Bletzinger, Eugenio Onate (Eds.), IASS Symposium 2019 - 60th Anniversary Symposium of the International Association for Shell and Spatial Structures; Structural Membranes 2019 - 9th International Conference on Textile Composites and Inflatable Structures, FORM and FORCE, Barcelona, 2019, pp. 807–814. https://www.academia.edu/41659790/Large_torsion_on_elastic_lamella_grid_structures.
[25] E. Schling, J. Schikore, Morphology of kinetic asymptotic grids, Towards Rad. Regener. (2023), https://doi.org/10.1007/978-3-031-13249-0_31.
[26] J. Schikore, Compliant Grids: Theory, Design and Realization, Doctoral Dissertation, Technical University of Munich, 2023, https://nbn-resolving.org/urn:nbn:de:bvb:91-diss-20230630-1695390-1-8 (accessed August 25, 2025).
[27] H. Pottmann, M. Eigensatz, A. Vaxman, J. Wallner, Architectural geometry, Comput. Graph. 47 (2015) 145–164, https://doi.org/10.1016/j.cag.2014.11.002.
[28] C. Jiang, C. Tang, M. Tomičí, J. Wallner, H. Pottmann, Interactive modeling of architectural freeform structures: Combining geometry with fabrication and statics, in: Advances in Architectural Geometry 2014, 2015, https://doi.org/10.1007/978-3-319-11418-7_7.
[29] Z. Wan, K. Crolla, E. Schling, Geometry-driven development of semi-compliant kinetic asymptotic structures, Adv. Eng. Inform. 68 (2025) 103762, https://doi.org/10.1016/j.aei.2025.103762.
[30] C. Tang, X. Sun, A. Gomes, J. Wallner, H. Pottmann, Form-finding with polyhedral meshes made simple, ACM Trans. Graph. (2014), https://doi.org/10.1145/2601097.2601213.
[31] M.A. Branch, T.F. Coleman, Y. Li, Subspace, interior, and conjugate gradient method for large-scale bound-constrained minimization problems, SIAM J. Scient. Comput. 21 (1999), https://doi.org/10.1137/S1064827595289108.
[32] J. Lienhard, Bending Active Structures: Form-finding Strategies using Elastic Deformation in Static and Kinematic Systems and the Structural Potentials Therein, Doctoral Thesis, 2014, p. 211, https://doi.org/10.18419/opus-107 (accessed March 17, 2023).
[33] Abaqus, Abaqus analysis user's manual, Abaqus 6 (12) (2012) 1.
[34] F. Laccone, L. Malomo, N. Pietroni, P. Cignoni, T. Schork, Integrated computational framework for the design and fabrication of bending-active structures made from flat sheet material, Structures 34 (2021) 979–994, https://doi.org/10.1016/j.istruc.2021.08.004.
[35] H. Rubin, Evaluierung der linearen und nichtlinearen Stabstatik in Theorie und Software. Prüfbeispiele, Fehlerursachen, genaue Theorie. Von G. Lumpe, V. Gensichen, Stahlbau 83 (2014), https://doi.org/10.1002/stab.201490107.